nature catalysis

ARTICLES

https://doi.org/10.1038/s41929-019-0416-2

Dry reforming of methane catalysed by molten metal alloys

Clarke Palmer[1], D. Chester Upham[2], Simon Smart[3], Michael J. Gordon[1], Horia Metiu[2] and Eric W. McFarland[1]*

Dry reforming of methane usually affords low-quality syngas with equimolar amounts of CO and H_2. Here we report the high conversion of CH_4 and CO_2 to syngas and solid carbon through simultaneous pyrolysis and dry reforming of methane in a bubble column reactor using a molten metal alloy catalyst (65:35 mol% Ni:In). The H_2 to CO ratio can be increased above 1:1 using feed ratios of CH_4:CO_2 greater than 1:1 to produce stoichiometric solid carbon as a co-product that is separable from the molten metal. A coupled reduction–oxidation cycle is carried out in which CO_2 is reduced by a liquid metal species (for example, In) and methane is partially oxidized to syngas by the metal oxide intermediate (for example, In_2O_3), regenerating the native metal. Moreover, the H_2:CO product ratio can be easily controlled by adjusting the CH_4:CO_2 feed ratio, temperature, and residence time in the reactor.

Dry reforming of methane (DRM) is a well-studied reaction to make syngas ($CO + H_2$), but it has not found commercial applications[1]. Nevertheless, interest in DRM has grown as researchers have sought ways to utilize CO_2 to obtain value-added products and to make use of high-CO_2-content natural gas deposits that cannot be economically used for steam reforming[2]. The biogas produced by anaerobic digestion of food, green waste, wastewater sludge or even municipal landfills has a high CO_2 content. In principle, DRM could be used to convert the CO_2 and CH_4 from these sources to more valuable syngas and might eliminate the need for costly CH_4–CO_2 separations[3].

Syngas for methanol or hydrocarbon production (via Fischer–Tropsch chemistry[4]) requires a H_2:CO feed ratio of 2:1. Syngas is currently produced by steam methane reforming (SMR) or autothermal reforming. These syngas production processes have shortcomings: SMR produces 10 tonnes of CO_2 per tonne of H_2 (ref. [2]), whereas autothermal reforming uses costly air separation to produce pure O_2 as a feedstock[5–8]. Although avoiding these same shortcomings, the DRM processes explored thus far can only produce low-value syngas with H_2:CO ratios of at most 1:1.

All syngas-producing processes are afflicted by coking. Coke formation is especially prominent in the DRM between 550–700 °C due to the Boudouard reaction ($2CO \rightleftharpoons C + CO_2$) and above 900 °C due to methane pyrolysis ($CH_4 \rightarrow C + 2H_2$) (see Supplementary Fig. 1 and Supplementary Table 1 for reaction thermodynamics)[9–11]. This necessitates periodic decoking of the catalyst by burning the carbon, which produces CO_2 as a by-product[6,10,12–14] and increases the cost of the process. Catalyst deactivation through sintering and unwanted solid-state reactions between the metallic catalyst and the oxide support also take place at elevated temperatures[15]. The current state-of-the-art reactor designs that attempt to mitigate these problems have focused on increasingly complex catalyst morphologies[16–19], plasma-assisted reactors[20,21], noble metal catalysts[22] or electrochemical routes[23,24] that have so far proven to be cost prohibitive for commercialization.

Molten metals and metal alloys have recently been shown to be highly effective catalysts and heat-transfer media for methane pyrolysis using bubble column reactors[25–30]. In this process, methane is decomposed into hydrogen and a low-density solid carbon by-product that floats on the surface of the melt, circumventing deactivation of the catalytic liquid and allowing for easy separation and removal of the carbon. Molten salt catalysts in bubble column reactors have also been proposed previously for the DRM[31–33], including designs that feed excess methane. However, in these cases, the temperatures for reaction were limited to <800 °C, effectively limiting methane pyrolysis and the H_2:CO ratio to less than 1:1 (ref. [33]). Molten nitrate[34] and molten carbonate[35] salts, which offer chemical looping possibilities, face stability issues well below methane pyrolysis temperatures[36]. Molten metals do not have these limitations.

Here we propose a process for syngas production from methane and CO_2 that is not affected by coking or sintering and allows control of the H_2:CO ratio in the syngas that is produced to directly suit the needs of various downstream processes. We use a molten metal catalyst in a bubble column reactor to avoid coking and sintering, operating at high temperatures so that dry reforming and methane pyrolysis take place simultaneously.

There are three advantages of this scheme. First, the H_2:CO product ratio can be controlled by varying the CH_4:CO_2 feed ratio. In particular, when using a 2:1 CH_4:CO_2 ratio, the process produces a valuable syngas with high conversion and selectivity in a 2:1 H_2:CO ratio, which is immediately suitable for methanol synthesis and Fischer–Tropsch production of higher hydrocarbons. In the current implementation of dry reforming, one cannot use an excess of CH_4 because of coking, which limits the H_2:CO ratio in the product to 1:1. Second, the process makes syngas by consuming CO_2, unlike SMR, which produces CO_2. Third, the solid carbon produced by the reaction floats to the surface of the melt where it can be removed. Each gas bubble in the bubble reactor is in contact with a carbon-free molten catalyst surface; as such, there is neither coking nor coarsening. In addition, the solid carbon co-product may be valuable for use in electrodes, material additives or activated carbons. If the amount of carbon produced would be too large to be

[1]Department of Chemical Engineering, University of California–Santa Barbara, Santa Barbara, CA, USA. [2]Department of Chemistry and Biochemistry, University of California–Santa Barbara, Santa Barbara, CA, USA. [3]School of Chemical Engineering, The University of Queensland, St Lucia, Queensland, Australia. *e-mail: ewmcfar@engineering.ucsb.edu

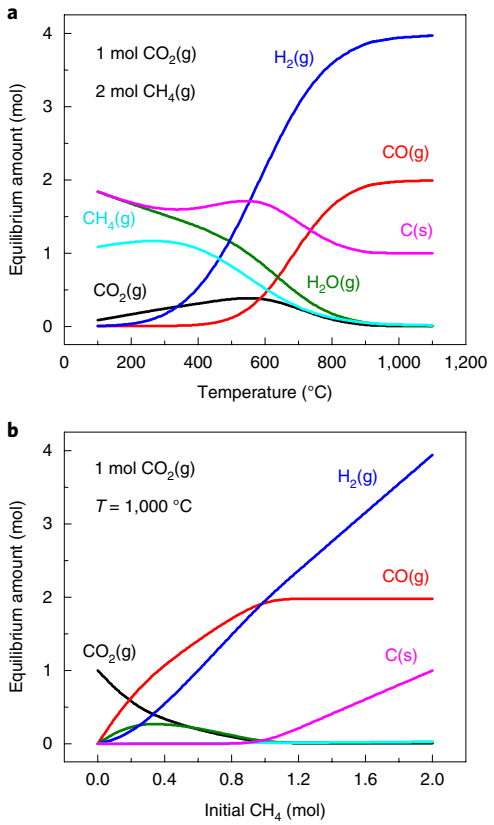

Fig. 1 | Calculated equilibrium compositions of DRM at 1 atm. **a**,**b**, A 2:1 CH_4:CO_2 molar ratio versus temperature (**a**) and 1 mol of CO_2 at 1,000 °C with differing initial moles of CH_4 (**b**).

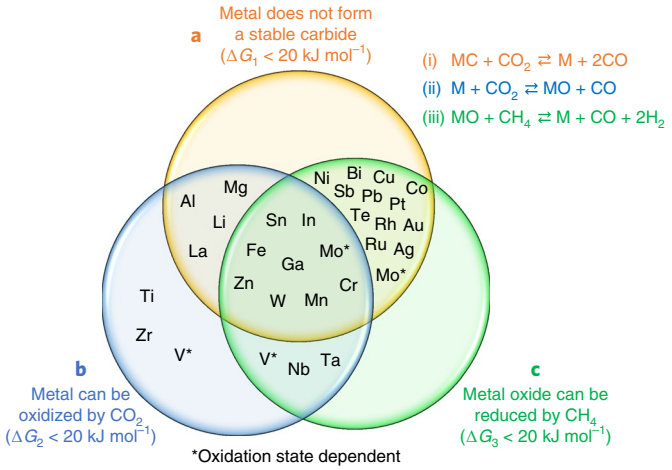

Fig. 2 | A summary of thermodynamic properties of eligible metal candidates for participation in a CH_4/CO_2 redox cycle for DRM. **a**,**b**, Criteria include: the metal carbide is unstable (**a**), the metal can be oxidized by CO_2 to all of the possible oxidation states (**b**) and all of the possible metal oxides can be reduced by CH_4 (**c**). Each thermodynamic criterion is met if the corresponding $\Delta G_{reaction}$ is less than +20 kJ mol^{-1} at 1,080 °C.

absorbed by the existing carbon markets, the carbon can be safely stored indefinitely at low cost, unlike the CO_2 produced by SMR.

We report calculations that identify In (among other metals) to be thermodynamically suitable for the proposed reaction scheme. We facilitate combined methane dry reforming and pyrolysis in a 65:35 mol% Ni:In molten metal bubble column reactor. We achieve a syngas product ratio that is >1:1 H_2:CO with a 2:1 CH_4:CO_2 feed ratio. We demonstrate the tunability of the desired syngas ratio by adjusting the CH_4:CO_2 feed ratio, reaction temperature and bubble residence time.

Results

Thermodynamic analysis. Thermodynamic calculations were performed using the online FactSage thermochemical databases[37] to determine the equilibrium composition as a function of the temperature and CH_4:CO_2 feed ratio (Fig. 1); we also examined the possibility that CO_2 might react with a metal species in the molten catalyst to form metal oxides. We found that certain oxides (for example, indium oxide) are not stable at equilibrium in the presence of methane and we therefore do not have to include them in the reaction network for equilibrium calculations; however, the metal oxides can form as intermediates when the reaction is run at steady state.

The results of the equilibrium calculations are shown in Fig. 1. Running these reactions at 1,000 °C, in excess of methane (that is, CH_4:CO_2 = 2:1, in Fig. 1a) and at atmospheric pressure is very favourable thermodynamically: CH_4 and CO_2 are completely converted and no water is present in the product. Figure 1b shows the benefit of using CH_4 in excess: CH_4 and CO_2 are completely converted, there is no water if equilibrium is reached and the H_2:CO product ratio can be increased at will by increasing the amount of CH_4. Hydrogen is produced by the simultaneous occurrence of the DRM and methane pyrolysis. Oyama et al. pointed out that the DRM is not competitive with SMR because the reverse water-gas shift reaction consumes the hydrogen in the feed to form water[38]. Fig. 1a shows that this is not the case under the equilibrium conditions proposed here. Increasing the pressure does result in lower conversions of CH_4 and CO_2 and an increased amount of H_2O present at equilibrium (Supplementary Fig. 2), but it is less H_2O compared to equilibrium compositions of the 1:1 CH_4:CO_2 feeds explored previously[37]. All of the experiments presented here were carried out at one atmosphere or less.

Thermodynamic calculations are also helpful for the selection of the molten metal catalyst. Assuming that the oxidation of the metal by CO_2 and the reduction of the metal oxide by CH_4 are part of the reaction mechanism, the metal(s) in the melt ought to satisfy three criteria at the desired operating temperature of 1,000–1,100 °C: (1) CO_2 must be able to oxidize one (or both) metals, (2) CH_4 must be able to reduce the metal oxide species formed and (3) the metals should not form stable carbides under the reaction conditions. The precipitation of metal carbide out of the melt would cause metal loss, which is not acceptable economically.

Thermodynamic calculations were used to find which metals satisfy these criteria. The results are summarized as a ternary Venn diagram in Fig. 2. The metals that satisfy these three criteria (namely, Sn, Zn, Fe, W, Ga, In, Mn and Cr) are the ones in the overlapping region of the three circles. It is worth highlighting that Fe, W, Mn and Cr normally form stable carbides under these conditions, but satisfy our criteria because CO_2 can react with the carbides to regenerate the metal (and form CO). The results were obtained by equilibrium calculations of reactions (i)–(iii) (shown in the figure). It is assumed that the thermodynamics of these reactions when the metal is in an alloy is the same as when the metals are pure.

A further criterion is that the metal or metal alloy should be molten at the reaction temperature. This is obviously not the case for pure W, Fe, Mn or Cr; however, these metals can be used as a molten catalyst in alloys with metals that have lower melting temperatures, such as alkali metals, alkaline earths metals, Zn, Cd, Hg, Al, Ga, In, Sn, Tl, Sn, Pb, Bi, Se or Te. Other factors can limit the use of some

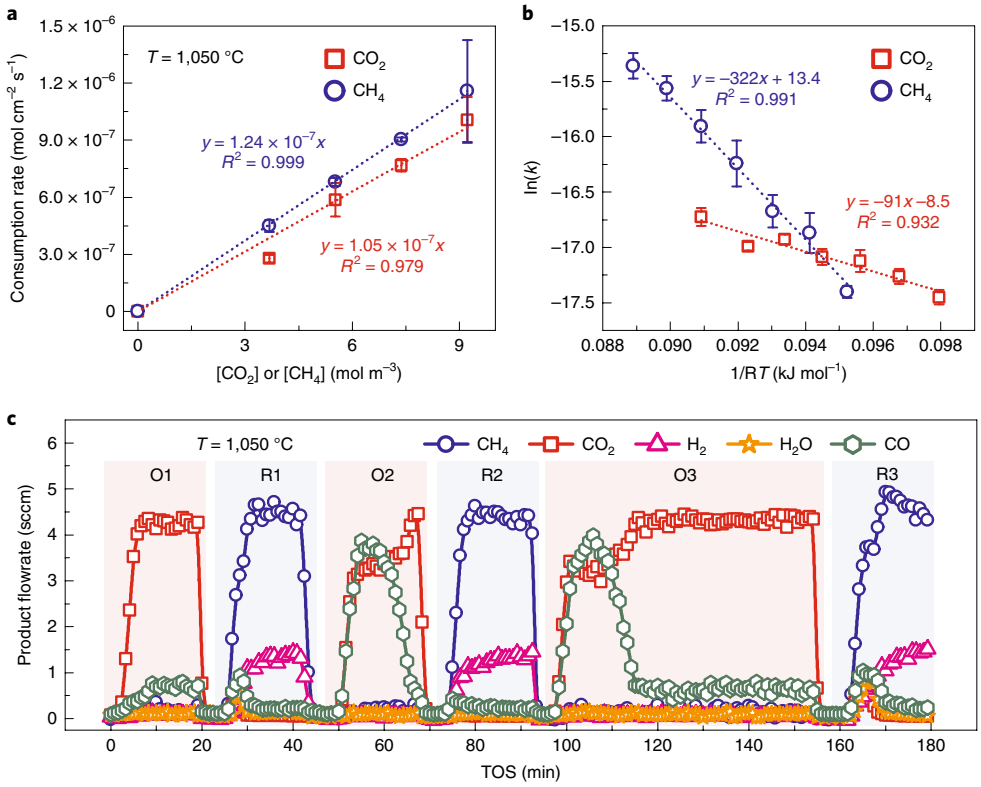

Fig. 3 | The differential reactor performance using ~0.39 cm² of a 65:35 mol% Ni:In molten metal alloy. a, The rate of CO_2 or CH_4 consumption versus $[CO_2]$ or $[CH_4]$ at 1,050 °C. The linearity of the plots confirms that the reaction order is one. **b**, Arrhenius plots for CO_2 and CH_4. **c**, Catalytic reduction–oxidation cycling at 1,050 °C; 5 sccm of CO_2 is used for the oxidation (O) steps and 5 sccm of CH_4 is used for the reduction (R) steps. Argon is used to purge the system between steps. Error bars represent the s.d. between three trials.

of these solvent metals; for example, Cd and Tl are toxic, and alkali metals, alkaline earth metals, Mg, Zn, Te, and even Pb have high vapour pressures and thus can be used in a reflux column where the vapour might be catalytically active, a possibility that has not been investigated here.

Methane can easily reduce the oxides of the metals that are commonly used as catalysts in methane chemistry (Ni, Pt, Rh, Ru and so on), but these metals do not reduce CO_2 under the conditions (see Fig. 2). Aluminium, La and metals of groups 1 and 2 form stable oxides that are not reduced by methane at the desired reaction temperatures. Although this analysis is the same for the multiple oxidation states of some metals, V and Mo meet or fail certain criteria depending on the specific oxidization state that forms; for example, Mo conditionally passes this analysis for MoO_3, but not MoO_2. Group 5 transition metals (V, Nb and Ta) have favourable redox properties, but form stable carbides. Iron and Mn also form carbides, but these can be oxidized by CO_2 to recover the metal. Overall, based on thermodynamic and practical constraints, Fe, Sn, In, Ga and Mn are promising candidates.

Molten metal alloy catalyst selection. Based on the thermodynamic analysis presented above, a preliminary screening of molten metal alloy candidates was performed in a bubble column reactor with a residence time of ~1 s at 1,080 °C, and with a stoichiometric feed of 2:1 CH_4:CO_2 (Supplementary Fig. 3 and Supplementary Note 1). Alloy compositions were chosen to be at the solubility limit of the high-melting metal in the low-melting metal at 925 °C; 65:35 mol% Ni:In had the highest CH_4 and CO_2 conversions of 44% and 81%, respectively, and will be the focus of this manuscript. Manganese-based melts may be of interest in future works as Mn is cheap and earth-abundant.

Differential reactor measurements. A differential reactor with a controlled catalytic liquid surface area was used to measure kinetic parameters (for example, reaction orders and effective activation energies; Supplementary Figure 5 and Supplementary Note 2), as has been described in previous in-house works[28,30]. These kinetic parameters were measured independently for CH_4 and CO_2 on a clean 65:35 mol% Ni:In surface. The reaction order was found to be one in both cases (Fig. 3a). The measured CO_2 activation energy is 91 ± 11 kJ mol^{-1} and the measured CH_4 effective activation energy is 322 ± 22 kJ mol^{-1} (Fig. 3b). This measured activation barrier for CH_4 is convoluted with the gas-phase activation energy of 360–420 kJ mol^{-1} (Supplementary Fig. 6); therefore, the activation energy of CH_4 on a 65:35 mol% Ni:In surface is <322 kJ mol^{-1}.

We cycled passing CO_2 and CH_4 through the differential reactor (Fig. 3c) to confirm that the proposed redox catalytic cycle involving a metal oxide intermediate (that is, In_2O_3) contributes to the observed activity in the 65:35 mol% Ni:In melt. First, CO_2 was passed through the reactor in oxidation step 1 (O1, Fig. 3c) and CO formation was observed, indicating the formation of a metal oxide (that is, In_2O_3). No CO_2 conversion was observed in the same reactor without the molten metal alloy present (Supplementary Fig. 6). Methane was then passed through the reactor in reduction step 1 (R1, Fig. 3c) and oxidized products (that is, CO, CO_2 and H_2O) were initially observed, signalling the reduction of the metal oxide. Carbon dioxide was passed through once again in oxidation step 2 (O2, Fig. 3c) and an accelerated rate of CO production (and CO_2 consumption) was initially observed, which was attributed to the reverse Boudouard reaction between CO_2 and the solid carbon (or solubilized carbon) produced from methane pyrolysis in the previous step (R1). The rate of CO production in oxidation step 2 decreases as the carbon is consumed. A similar behaviour is

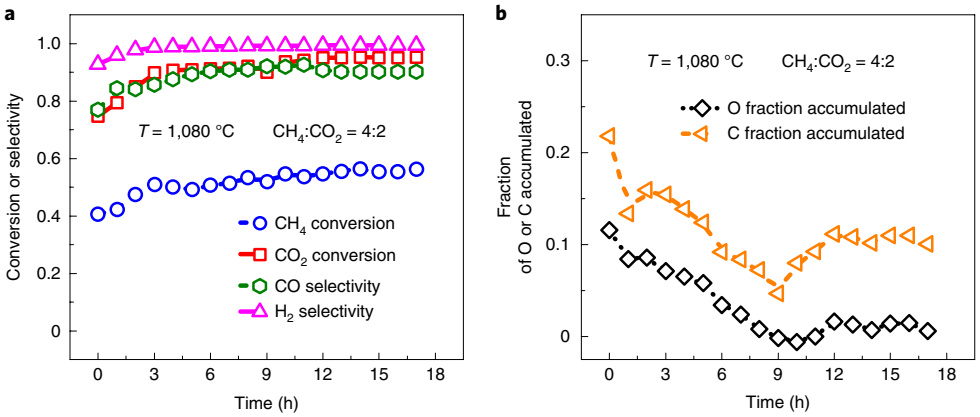

Fig. 4 | The DRM in a 65:35 mol% Ni:In molten metal bubble column reactor for a 2:1 CH_4:CO_2 feed at 1,080 °C and 0.4 atm methane over time. **a**,**b**, Reactant fractional conversions and product selectivities (**a**) and the fraction of C or O species accumulated versus time (**b**). The fraction of accumulated species is defined as the moles of species accumulated divided by the total moles of that species consumed from the reactant feed. The total reactor pressure was 1 atm.

observed in oxidation step 3 (O3, Fig. 3c), which is three times longer than oxidation step 2 to demonstrate that more oxidized products are produced in the subsequent reduction step, R3.

These experimental observations and mechanistic implications are consistent with the works by Otsuka et al., who explored the production of CO from CO_2 and H_2 from H_2O via an In_2O_3–In, reduction–oxidation cycle[39–45]. Specifically, CO_2 was demonstrated to be a successful oxidant for liquid In metal[44] and, although never experimentally explored, methane was acknowledged as a potential reductant for In_2O_3 as well[45].

Bubble column reactor performance. The differential reactor set-up described herein allowed for more reliable kinetic measurements; however, a molten metal bubble column is advantageous to achieve higher reactant conversions without deactivation due to the formation of solids (for example, metal oxides or carbon). A catalyst stability test was therefore performed for a 2:1 CH_4:CO_2 feed at 1,080 °C over the course of 17 h in a 65:35 mol% Ni:In bubble column (Fig. 4). The conversion of both CH_4 and of CO_2 increased gradually for the first 10 h and then levelled off for the next 7 h at 56 ± 2% molar conversion of CH_4 and 95 ± 2% for CO_2 (Fig. 4a). We have determined the oxygen retention (that is, the difference between the oxygen mass in the effluent and the oxygen mass in the intake) in the melt from the oxygen mass balance (see Fig. 4b). As expected, the retention is largest initially, decays with time and levels off to zero after ~9 h. This levelling happens because the rate of In_2O_3 production becomes equal to that of In_2O_3 consumption and the indium oxide concentration reaches a steady state, at which point no net oxygen is retained.

The selectivity to CO increases over the initial 9-h period from 0.78 to 0.9 ± 0.02, presumably because CO is produced from CO_2 reacting with carbon via the reverse Boudouard reaction ($CO_2 + C \rightarrow 2CO$; Supplementary Note 3) and CH_4 reacting with indium oxide ($CH_4 + 1/3In_2O_3 \rightarrow CO + 2H_2 + 2/3In$), leading to both carbon and oxide accumulation in the system. The selectivity to H_2 increases rapidly and levels off at 1.0 ± 0.02 after a short time (Fig. 4a).

Measurements of the dependence of the reaction products on the CH_4:CO_2 inlet feed ratio, temperature and residence time for the 65:35 mol% Ni:In melt are shown in Fig. 5. It is clear that the H_2:CO ratio decreases as more CO_2 is introduced into the feed (Fig. 5a). For CH_4:CO_2 feed ratios at or below 4:2, the H_2:CO syngas ratio is larger than 1, even for incomplete conversions of both CH_4 and CO_2 (Fig. 5a). It is important to note the appreciable CH_4 conversion that is observed for a pure methane feed (Fig. 5d); this activity is necessary to produce H_2-rich syngas product streams at longer residence times when the CO_2 is fully consumed.

The selectivity to H_2 is ~1 with pure methane and minimally depends on the introduction of CO_2. The H_2 selectivity was observed to be 0.97 at a feed composition of 1:1 CH_4:CO_2 (4:4, Fig. 5a); we attribute the high H_2 selectivity to rapid reduction of water at these reaction conditions by CH_4, C and/or In (Supplementary Note 4). The selectivity to CO is poor at high CH_4:CO_2 feed ratios due to a dominance of solid carbon over CO as the final product; CO selectivity increases when there is more CO_2 in the feed due to promotion of the reverse Boudouard reaction (Fig. 5a). Furthermore, more CO is produced from the reduction of In_2O_3 by CH_4 at larger CO_2 feed compositions, as demonstrated by the increase in CH_4 conversion (Fig. 5d).

The CO selectivity increases as the temperature is decreased below 1,080 °C, suggesting that the formation of CO is kinetically favoured over C and In_2O_3. The H_2:CO syngas product ratio decreases while still maintaining a selectivity to H_2 of 1 for a 2:1 CH_4:CO_2 feed ratio (Fig. 5b). The overall production rate of syngas decreases with decreasing temperature, visualized as a decrease in the conversions of CH_4 and CO_2 (Fig. 5e).

The residence time and temperature dependencies of the DRM performance in the Ni–In melt are similar (Fig. 5c,f). The bubble rise velocity was estimated to be ~15 cm s^{-1}, resulting in a residence time of ~0.9 s at the maximum depth of 13.5 cm. The results presented for a depth of 0 cm are collected when the inlet tube is situated just above the melt surface; the low conversions of CH_4 and CO_2 of 9% and 16% (Fig. 5f), respectively, are from surface and headspace reactions, confirming that reactions in the molten alloy are responsible for most of the observed activity at longer residence times.

Carbon characterization. After cooling, solid carbon is easily removed from the surface of the solidified melt. Unlike the loose graphitic powder that Upham and colleagues reported collecting from the surface of a 27:73 mol% Ni:Bi alloy after hours of methane pyrolysis[28], the carbon collected after hours of combined DRM and methane pyrolysis with 65:35 mol% Ni:In alloy had microscale polycrystalline structures (Fig. 6a).

Despite heterogeneity in the large-scale morphologies of the carbon structures, the small-scale individual building units appear to be homogenous. These nanometre-scale carbon crystallite units, for example, constitute the tips of the carbon brush-like structures (Fig. 6b). The D/G ratio >2 and G position between

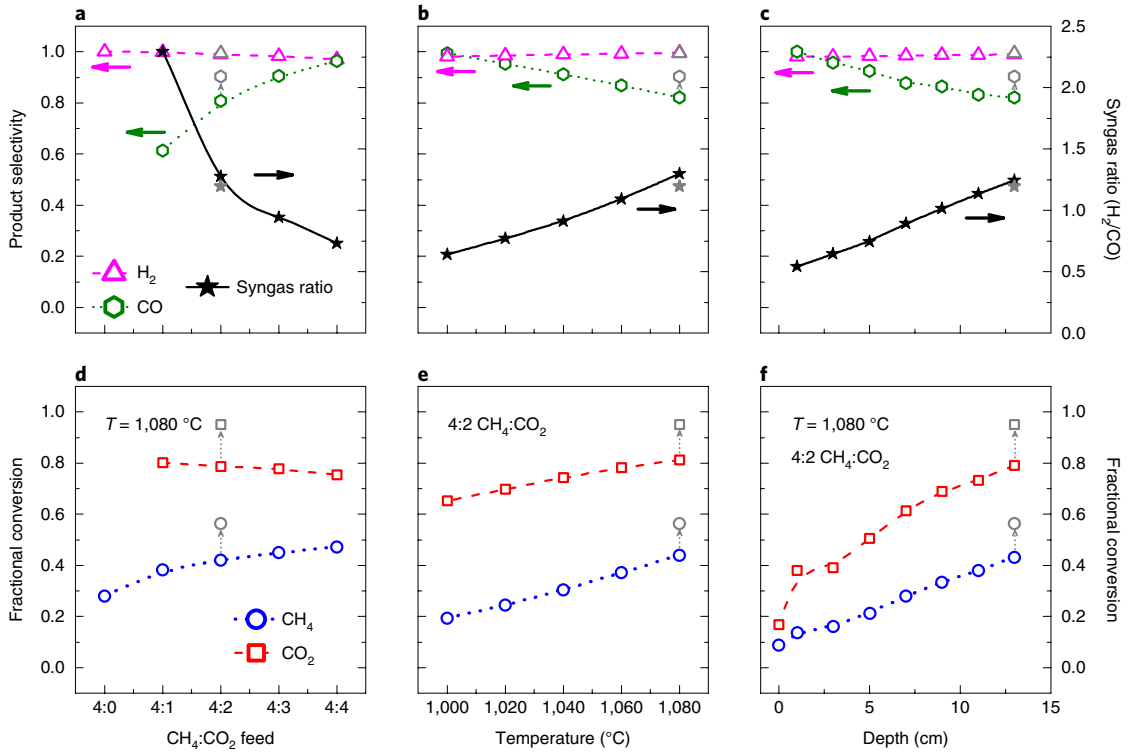

Fig. 5 | Reaction performance in a 65:35 mol% Ni:In molten alloy on the approach to steady-state operation. a–f, H_2 selectivity (pink triangles), CO selectivity (green hexagons) and the H_2:CO syngas ratio (black stars) are reported versus the CH_4:CO_2 feed (**a**), temperature (**b**) and depth (that is, residence time) (**c**). The corresponding conversions of CH_4 (red squares) and CO_2 (blue circles) are also shown (**d–f**). Steady-states values from Fig. 4 are plotted as grey data points. The methane partial pressure was 0.4 atm for all of the experimental conditions. The total reactor pressure was 1 atm. The depth of the gas inlet tube into the melt was 13.5 cm, except for panels (**c**) and (**f**).

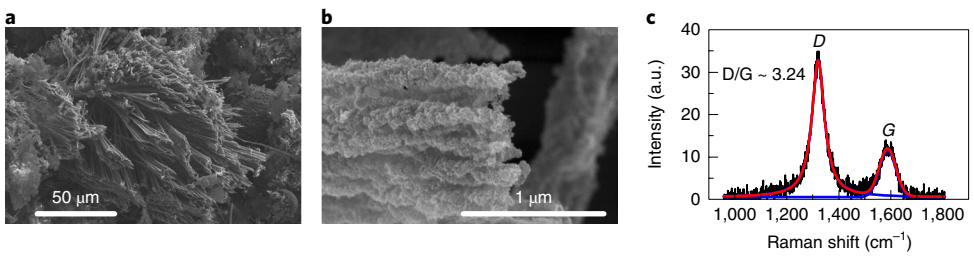

Fig. 6 | Characterization of carbon collected from the surface of a 65:35 mol% Ni:In solidified alloy after DRM. a, A micrograph showing bouquet of polycrystalline carbon brushes. **b**, An enlarged micrograph of carbon brush tips with individual carbon crystallite building units visible. **c**, A Raman spectrum of carbon with a *D*/*G* ratio of ~3.24. The *D* and *G* bands highlighted correspond to edge (that is, disordered) carbon domains and graphitic domains, respectively.

1,580–1,600 cm^{-1} observed in the carbon's Raman spectrum (Fig. 6c) is characteristic of sp^2 nanocrystalline graphite[46,47]. Graphitic carbons are more resistant to oxidation and gasification than less-ordered carbon morphologies[48]. The carbon species gasified to CO via the reverse Boudouard reaction are therefore probably intermediate and/or amorphous carbons that are formed from methane decomposition, whereas the graphitic species accumulate at the surface of the bubble column.

Conclusions

The coupling of methane dry reforming with catalytic methane pyrolysis in a molten metal bubble column reactor overcomes the limitations of traditional DRM solid catalysts; namely, deactivation by coking, metal sintering at high temperatures and syngas product ratios that are limited to a ratio of 1:1 H_2:CO. The syngas product ratio can be easily controlled in the process described here by varying the inlet feed ratio of CH_4:CO_2, temperature and gas residence time.

The process developed in this work may be particularly useful for conversion of high-CO_2-content natural gas feedstocks that cannot be processed via conventional steam reforming, as well as processing biogas from various sources. It may also be used to convert the CO_2 produced by various industrial processes to useful chemicals, making these processes carbon-neutral and avoiding the need for sequestration.

Methods

Molten alloy preparation and DRM experimentation. Bulk metals were purchased as individual millimetre shots (>99.9% purity) from Sigma-Aldrich and Fisher Scientific for all of the experiments. Gases from Airgas tanks were delivered to the system by MKS 1179 mass flow controllers; 6A ceramic fibre furnaces from

Watlow were used to heat the reactors. The outlet of the reactor was attached to Teflon lines wrapped in heating tape kept above 120 °C. A heated glass capillary tube sampled from the product stream and fed to an online, 300 AMU residual gas analyser (quadrupole mass spectrometer) from Stanford Research Systems.

Metal shots were weighed and loaded into 12 mm outside diameter (OD), 10 mm interior diameter (ID) quartz reactors for the bubble column experiments. The loaded reactor was situated in the ceramic furnace with 30 sccm of argon and 5 sccm of hydrogen purging the headspace. The ceramic furnace was heated to well above the melting point of the desired alloy and further metal shots were added to increase the liquid metal height to ~14 cm. The quartz reactor was sealed with ground glass ball-and-socket joints; 5 sccm of hydrogen and 5 sccm of argon were bubbled up through the bottom of the melt using a 3 mm OD, 2 mm ID quartz inlet tube to reduce any metal oxide species and ensure that the alloy was well mixed. The total bubbling flowrate during experiments was 10 sccm; the methane flowrate was 4 sccm (supplemented with argon or CO_2 where noted). Details of the experimental set-up are shown in Supplementary Fig. 3.

Small ceramic crucibles (Cs Ceramic, 8 mm OD, 5 mm height) were filled with desired metal compositions and melted in a large tube furnace under a mixed hydrogen and argon flow (7 sccm hydrogen and 40 sccm argon) for the differential reactor experiments. Single crucibles were then loaded into the bottom of a small quartz reactor (12 mm OD, 10 mm ID). A quartz inlet tube (8 mm OD, 1 mm ID) was inserted into the reactor with the outlet of the inlet tube situated just above the surface of the crucible. The calculated melt surface area was ~0.39 cm^2. Details of the experimental set-up are shown in Supplementary Fig. 5. Initially, 2.5 sccm of argon and 2.5 sccm of hydrogen were flowed while the reactor was heated to 1,000 °C or 1,100 °C to reduce any metal oxides. The reactor was purged with 2.5 sccm of argon when no hydrogen conversion was observed. For the rate order determination (results shown in Fig. 3a), the reaction temperature was 950 °C and the concentrations of CO_2 or CH_4 were adjusted by supplementing the feed with argon; the total flowrate was always 10 sccm. The temperature was altered between 950 and 1050 °C for the Arrhenius plot determination (shown in Fig. 3b). For CO_2, the flowrate was 5 sccm of CO_2 and no argon was used. For CH_4, 5 sccm of CH_4 and 5 sccm of argon was used. Details of the kinetic calculations for these experiments are described in Supplementary Note 2.

Reactor performance evaluation metrics.

$$\text{Hydrogen Selectivity } (S_{H_2}) = \frac{\text{moles } H_2 \text{ produced}}{2\times \text{moles } CH_4 \text{ consumed}} \quad (1)$$

$$\text{CO Selectivity } (S_{CO}) = \frac{\text{moles CO produced}}{\text{moles } CH_4 \text{ consumed} + \text{moles } CO_2 \text{ consumed}} \quad (2)$$

$$\text{Fraction of O accumulated} = \frac{\text{moles of O produced as } In_2O_3}{2\times \text{moles } CO_2 \text{ consumed}} \quad (3)$$

$$\text{Fraction of C accumulated} = \frac{\text{moles of solid C produced}}{\text{moles } CH_4 \text{ consumed} + \text{moles } CO_2 \text{ consumed}} \quad (4)$$

Carbon characterization. Scanning electron micrographs are taken on a FEI Nova Nano 650 SEM, equipped with an EDT detector. Images were taken at an accelerating voltage of 5 kV at multiple magnifications. Samples were adhered to titanium SEM stages with adhesive copper tape and sputter coated with Au–Pd to ensure conductivity and prevent charging. Raman spectra were obtained from a Horiba LabRAM ARAMIS equipped with a 633 nm laser.

Data availability

The data that support the plots within this paper and other findings of this study are available from the corresponding author on reasonable request.

Received: 11 June 2019; Accepted: 29 November 2019;
Published online: 20 January 2020

References

1. Pakhare, D. & Spivey, J. A review of dry (CO_2) reforming of methane over noble metal catalysts. *Chem. Soc. Rev.* **43**, 7813–7837 (2014).
2. Agrafiotis, C., von Storch, H., Roeb, M. & Sattler, C. Solar thermal reforming of methane feedstocks for hydrogen and syngas production—a review. *Renew. Sustain. Energy Rev.* **29**, 656–682 (2014).
3. Lau, C. S., Tsolakis, A. & Wyszynski, M. L. Biogas upgrade to syn-gas (H_2–CO) via dry and oxidative reforming. *Int. J. Hydrog. Energy* **36**, 397–404 (2011).
4. Henrici-Olivé, G. & Olivé, S. The Fischer–Tropsch synthesis: molecular weight distribution of primary products and reaction mechanism. *Angew. Chem. Int. Ed.* **15**, 136–141 (1976).
5. Smith, A. R. & Klosek, J. A review of air separation technologies and their integration with energy conversion processes. *Fuel Process. Technol.* **70**, 115–134 (2001).
6. Rostrup-Nielsen, J. R., Sehested, J. & Nørskov, J. K. Hydrogen and synthesis gas by steam- and CO_2 reforming. *Adv. Catal.* **47**, 65–139 (2002).
7. Bradford, M. C. J. & Vannice, M. A. CO_2 reforming of CH_4. *Catal. Rev. Sci. Eng.* **41**, 1–42 (1999).
8. Horn, R. & Schlogl, R. Methane activation by heterogeneous catalysis. *Catal. Lett.* **145**, 23–29 (2015).
9. Nikoo, M. K. & Amin, N. A. S. Thermodynamic analysis of carbon dioxide reforming of methane in view of solid carbon formation. *Fuel Process. Technol.* **92**, 678–691 (2011).
10. Rostrup-Nielsen, J. R. Industrial relevance of coking. *Catal. Today* **37**, 225–232 (1997).
11. Li, Y., Wang, Y., Zhang, X. & Mi, Z. Thermodynamic analysis of autothermal steam and CO_2 reforming of methane. *Int. J. Hydrog. Energy* **33**, 2507–2514 (2008).
12. Rostrup-Nielsen, J. R. Production of synthesis gas. *Catal. Today* **18**, 305–324 (1993).
13. Song, C. S. & Wei, P. Tri-reforming of methane: a novel concept for catalytic production of industrially useful synthesis gas with desired H_2/CO ratios. *Catal. Today* **98**, 463–484 (2004).
14. Aasberg-Petersen, K. et al. Natural gas to synthesis gas—catalysts and catalytic processes. *J. Nat. Gas. Sci. Eng.* **3**, 423–459 (2011).
15. Fan, M. S., Abdullah, A. Z. & Bhatia, S. Catalytic technology for carbon dioxide reforming of methane to synthesis gas. *ChemCatChem* **1**, 192–208 (2009).
16. Li, Z., Mo, L., Kathiraser, Y. & Kawi, S. Yolk–satellite–shell structured Ni–yolk@Ni@SiO_2 nanocomposite: superb catalyst toward methane CO_2 reforming reaction. *ACS Catal.* **4**, 1526–1536 (2014).
17. Kim, S. M. et al. Cooperativity and dynamics increase the performance of NiFe dry reforming catalysts. *J. Am. Chem. Soc.* **139**, 1937–1949 (2017).
18. Li, X. Y. et al. Dry reforming of methane over Ni/La_2O_3 nanorod catalysts with stabilized Ni nanoparticles. *Appl. Catal. B* **202**, 683–694 (2017).
19. Das, S. et al. Silica–ceria sandwiched Ni core-shell catalyst for low temperature dry reforming of biogas: coke resistance and mechanistic insights. *Appl. Catal. B* **230**, 220–236 (2018).
20. Tu, X. & Whitehead, J. C. Plasma-catalytic dry reforming of methane in an atmospheric dielectric barrier discharge: understanding the synergistic effect at low temperature. *Appl. Catal. B* **125**, 439–448 (2012).
21. Tu, X. & Whitehead, J. C. Plasma dry reforming of methane in an atmospheric pressure AC gliding arc discharge: co-generation of syngas and carbon nanomaterials. *Int. J. Hydrog. Energy* **39**, 9658–9669 (2014).
22. Yagi, F. et al. in *Studies in Surface Science and Catalysis* (eds Noronha, F. B. et al.) Vol. 167, 385–390 (Elsevier, 2007).
23. Zhang, P., Tong, J. & Huang, K. Combining electrochemical CO_2 capture with catalytic dry methane reforming in a single reactor for low-cost syngas production. *ACS Sustain. Chem. Eng.* **4**, 7056–7065 (2016).
24. Lu, J. et al. Highly efficient electrochemical reforming of CH_4/CO_2 in a solid oxide electrolyser. *Sci. Adv.* **4**, eaar5100 (2018).
25. Steinberg, M. Fossil fuel decarbonization technology for mitigating global warming. *Int. J. Hydrog. Energy* **24**, 771–777 (1999).
26. Geißler, T. et al. Experimental investigation and thermo-chemical modeling of methane pyrolysis in a liquid metal bubble column reactor with a packed bed. *Int. J. Hydrog. Energy* **40**, 14134–14146 (2015).
27. Plevan, M. et al. Thermal cracking of methane in a liquid metal bubble column reactor: experiments and kinetic analysis. *Int. J. Hydrog. Energy* **40**, 8020–8033 (2015).
28. Upham, D. C. et al. Catalytic molten metals for the direct conversion of methane to hydrogen and separable carbon. *Science* **358**, 917–921 (2017).
29. Wang, K., Li, W. S. & Zhou, X. P. Hydrogen generation by direct decomposition of hydrocarbons over molten magnesium. *J. Mol. Catal. A* **283**, 153–157 (2008).
30. Palmer, C. et al. Methane pyrolysis with a molten Cu–Bi alloy catalyst. *ACS Catal.* **9**, 8337–8345 (2019).
31. Kodama, T., Koyanagi, T., Shimizu, T. & Kitayama, Y. CO_2 reforming of methane in a molten carbonate salt bath for use in solar thermochemical processes. *Energy Fuels* **15**, 60–65 (2001).
32. Gokon, N., Oku, Y., Kaneko, H. & Tamaura, Y. Methane reforming with CO_2 in molten salt using FeO catalyst. *Sol. Energy* **72**, 243–250 (2002).
33. Al-Ali, K., Kodama, S. & Sekiguchi, H. Modeling and simulation of methane dry reforming in direct-contact bubble reactor. *Sol. Energy* **102**, 45–55 (2014).
34. Alberto, G. et al. Solar steam reforming of natural gas for hydrogen production using molten salt heat carriers. *AIChE J.* **54**, 1932–1944 (2008).

35. Kodama, T., Gokon, N., Inuta, S.-i, Yamashita, S. & Seo, T. Molten-salt tubular absorber/reformer (MoSTAR) project: the thermal storage media of Na_2CO_3–MgO composite materials. *J. Sol. Energy Eng.* **131**, 041013–041013-8 (2009).
36. Kodama, T., Isobe, Y., Kondoh, Y., Yamaguchi, S. & Shimizu, K. I. Ni/ceramic/molten-salt composite catalyst with high-temperature thermal storage for use in solar reforming processes. *Energy* **29**, 895–903 (2004).
37. Bale, C. W. et al. FactSage thermochemical software and databases. *Calphad* **54**, 35–53 (2010-2016).
38. Oyama, S. T., Hacarlioglu, P., Gu, Y. & Lee, D. Dry reforming of methane has no future for hydrogen production: comparison with steam reforming at high pressure in standard and membrane reactors. *Int. J. Hydrog. Energy* **37**, 10444–10450 (2012).
39. Otsuka, K., Yasui, T. & Morikawa, A. Reproducible hydrogen production from water by indium oxide. *J. Catal.* **72**, 392–393 (1981).
40. Otsuka, K., Takizawa, Y., Shibuya, S.-i & Morikawa, A. Hydrogen production from water by In_2O_3 and K_2CO_3 using graphite, active carbon and biomass as reductants. *Chem. Lett.* **10**, 347–350 (1981).
41. Otsuka, K., Takizawa, Y. & Morikawa, A. Hydrogen production from water on carbon-reduced indium oxide. *Fuel Process. Technol.* **6**, 215–223 (1982).
42. Otsuka, K., Yasui, T. & Morikawa, A. The decomposition of water on the CO- or H_2-reduced indium oxide. *Bull. Chem. Soc. Jpn* **55**, 1768–1771 (1982).
43. Otsuka, K., Shibuya, S.-i & Morikawa, A. Effective supported-In_2O_3 for the production of hydrogen from water by the reduction-oxidation cycle of In_2O_3. *Chem. Lett.* **11**, 987–990 (1982).
44. Otsuka, K., Yasui, T. & Morikawa, A. Production of CO from CO_2 by reduced indium oxide. *J. Chem. Soc. Faraday Trans.* **78**, 3281–3286 (1982).
45. Otsuka, K., Shibuya, S.-I. & Morikawa, A. Role of carriers in the production of hydrogen from water by reduction-oxidation cycle of In_2O_3. *J. Catal.* **84**, 308–316 (1983).
46. Jerng, S. K. et al. Nanocrystalline graphite growth on sapphire by carbon molecular beam epitaxy. *J. Phys. Chem. C* **115**, 4491–4494 (2011).
47. Ferrari, A. C. & Robertson, J. Raman spectroscopy of amorphous, nanostructured, diamond–like carbon, and nanodiamond. *Philos. Trans. R. Soc. Lond. A* **362**, 2477–2512 (2004).
48. Pinilla, J. L. et al. Hydrogen production by thermo-catalytic decomposition of methane: regeneration of active carbons using CO_2. *J. Power Sources* **169**, 103–109 (2007).

Acknowledgements

Funding to support this work was provided by the Energy & Biosciences Institute through the EBI-Shell programme. Support for S.S. was provided by the Dow Centre for Sustainable Engineering Innovation at the University of Queensland. We made use of Center for Scientific Computing at the California NanoSystems Institute funded in part by NSF CNS-0960316 and Hewlett-Packard. The MRL Shared Experimental Facilities are supported by the MRSEC Program of the NSF under award no. DMR 1720256; a member of the NSF-funded Materials Research Facilities Network (www.mrfn.org). The authors are grateful for the indispensable technical assistance of R. Bock of the UCSB Chemistry Department, who prepared all of the quartz reactor components and their modifications.

Author contributions

C.P., D.C.U. and E.W.M. conceived the research. C.P. performed the thermodynamic analysis in the main manuscript, experimental work and carbon characterizations, with contributions and feedback from S.S., E.W.M., M.J.G. and H.M. S.S. performed the supplemental thermodynamic analysis. C.P. prepared the data figures. All authors contributed to the written text and data analysis.

Competing interests

The authors declare no competing interests.

Additional information

Supplementary information is available for this paper at https://doi.org/10.1038/s41929-019-0416-2.

Correspondence and requests for materials should be addressed to E.W.M.

Reprints and permissions information is available at www.nature.com/reprints.

Publisher's note Springer Nature remains neutral with regard to jurisdictional claims in published maps and institutional affiliations.